IEEE Access
Multidisciplinary | Rapid Review | Open Access Journal

Received December 22, 2017, accepted January 28, 2018, date of publication February 8, 2018, date of current version March 19, 2018.

Digital Object Identifier 10.1109/ACCESS.2018.2803788

INVITED PAPER

Multiple Drone-Cell Deployment Analyses and Optimization in Drone Assisted Radio Access Networks

WEISEN SHI[1], JUNLING LI[1], WENCHAO XU[1], HAIBO ZHOU[2], NING ZHANG[3], SHAN ZHANG[4], (Member, IEEE), AND XUEMIN SHEN[1], (Fellow, IEEE)

[1]Department of Electrical and Computer Engineering, University of Waterloo, Waterloo, ON N2L 3G1, Canada
[2]School of Electronic Science and Engineering, Nanjing University, Nanjing 210023, China
[3]Department of Computing Science, Texas A&M University–Corpus Christi, Corpus Christi, TX 78412, USA
[4]School of Computer Science and Engineering, Beihang University, Beijing 100191, China

Corresponding author: Shan Zhang (zhangshan2007@gmail.com)

This work was supported in part by the National Natural Science Foundation of China under Grant 91638204 and in part by the Natural Sciences and Engineering Research Council, Canada.

ABSTRACT In this paper, we propose a drone assisted radio access networks architecture in which drone-cells are leveraged to relay data between base stations and users. Based on the state-of-the-art drone-to-user and drone-to-base station (D2B) channel models, we first analyze the user coverage and the D2B backhaul connection features of drone-cells. We then formulate the 3-D drone-cell deployment problem with the objective of maximizing the user coverage while maintaining D2B link qualities, for a given number of drone cells being deployed. To solve the problem, the particle swarm optimization (PSO) algorithm is leveraged for its low computational cost and unique features suiting the spatial deployment of drone-cells. We propose a per-drone iterated PSO (DI-PSO) algorithm that optimizes drone-cell deployments for different drone-cell numbers, and prevents the drawbacks of the pure PSO-based algorithm derived from related works. Simulations show that the DI-PSO algorithm can achieve higher coverage ratio with less complexity comparing to the pure PSO-based algorithm.

INDEX TERMS Drone, drone communication, radio access networks, particle swarm optimization, D2U, D2B.

I. INTRODUCTION

Providing ubiquitous connectivity for users and devices with diversified service requirements is regarded as one of the key challenges in 5G networks [1]. To support the reliable and low-latency access of massive mobile users, considerable level of flexible deployment is required for future Radio Access Networks (RAN). However, current Base Stations (BSs) and Remote Radio Heads (RRHs) are deployed in certain geographical locations according to long-term traffic behaviors with little flexibility to be re-deployed. Such rigid RANs are reluctant to maintain ubiquitous connectivity for most 5G scenarios where dynamic data traffic occurs in both spatial and temporal domains [2]. Though densely deploying BSs or RRHs is one intuitive way to improve the RAN coverage, the high expenditure and low efficiency brought by this method are unacceptable for RAN operators [1]. To enhance RAN's flexibility for supporting massive dynamic connections, the emerging drone-cell communication technology is a promising solution.

Promoted by the well-developed flying control technologies and various commercial drone products, both academia and industry are devoting increasing number of efforts on the drone communication research [3]. Equipped with specific wireless modules and controlled by corresponding controllers (e.g. edge servers on BSs), flying drones can perform as drone-cells to provide temporal and on-demand communication services for areas of interests [4]. Comparing with legacy BSs, there are two advantages using drone-cells:

1) Line-of-Sight (LoS) Connection: Compared with ground BSs, drone-cells flying in the air have higher probability to connect ground users via LoS links, which facilitates highly reliable communications [5]. This advantage is further enhanced by drone-cell's mobility feature that allows 3D adjustments of the drone-cell position to avoid obstacles

between Drone-to-User (D2U) links [6]. For the Drone-to-BS (D2B) links, since the flying height of drone-cells can be close to the height of BS antennas, the D2B connections are naturally LoS with little probability to be blocked by tall buildings [7].

2) Dynamical Deployment: Different from traditional BSs which are statically fixed on dedicated locations, drones can be dynamically deployed according to real-time requirements, and allocated to different users or controllers on demands. Two types of control methods are considered in drone-cell deployments: 1) All drone-cells connect with corresponding central BSs taking charge of deployment control, which is similar to the Cloud-RAN (C-RAN) architecture while the RRHs functions are performed by flying drone-cells [8]; and 2) A swarm of drone-cells form a Flying Ad Hoc Network (FANET) and negotiate with each other to determine the deployment results. This method is mainly used in scenarios lacking of infrastructures, such as post-disaster communication recovery [9].

Recently there is significant effort to investigate drone-cell's potential to improve the performance of RAN. Through field experiments, Dhekne *et al*. demonstrate drone-cell's capability of improving the signal strength in coverage holes when they perform as the aerial extensions of BSs [10]. In [11], Zhang and Zhang study the spectrum sharing of Drone-Small-Cells (DSCs) network modeled by the 3D Poisson point process, and find the optimal density of DSCs to maximize the network throughput while satisfying the cellular network efficiency constraint. To maximize the minimum downlink throughput over ground users, Wu *et al*. formulate a mixed integer non-convex optimization problem in which the multi-user communication scheduling and association are jointly optimized with drone-cells trajectory and power control [3]. Block coordinate descent and successive convex optimization techniques are used for solving the problem. In [12], Al-Hourani *et al*. build an Air-to-Ground (A2G) pathloss model for low altitude platforms including drone-cells. A close-form expression of A2G pathloss model is proposed in which the probabilities of both LoS and Non-Line-of-Sight (NLoS) A2G links in different scenarios are considered. In its extension work, a D2B pathloss model for suburban scenario is formulated by Al-Hourani and Gomez [7] based on massive field experiments data. The model indicates a trade-off in the channel performance as the vertical angle between the drone-cell and the BS increases. Leveraging the pathloss model in [12], some researchers focus on exploring the optimal drone-cell deployment that maximizes specific performance metrics. In [13], Mozaffari *et al*. design a clustering approach to find the optimal trajectories and locations of drone-cells that maximize the information collection gain from ground Internet of Things (IoT) devices. Yang *et al*. propose a holistic framework using drone-cells to assist 5G networks in flash crowd traffic scenarios, and design a "first-selfish and second-share" method for drone-cell deployments [14]. Bor-Yaliniz *et al.* [15] formulate the 3D placement problem for single drone-cell as a Mixed-Integer Nonlinear Programming (MINLP) problem, and solve it through bisection search algorithm. Kalantari *et al.* [16] further explore the deployment of multiple drone-cells, and find the minimum number of drone-cells for dedicated coverage constraint by using Particle Swarm Optimization (PSO) algorithm. An optimal drone-cell placement algorithm maximizing the number of covered users with minimum power consumptions was designed by Alzenad *et al*., in which the drone-cell deployment problem is decoupled in the vertical and horizontal dimensions and solved respectively.

Although various approaches are proposed to optimize the deployment of drone-cells, the D2B communication is ignored or idealized in many works. Since the ultimate purpose of introducing drone-cells into RAN is enhancing users' accessibility to network services, it is inevitable to consider D2B communications and ensure their reliability in drone-cell deployments. Therefore, the 3D drone-cell deployment problem is not only affected by user distributions, but also constrained by the qualities of D2B links. In this paper, we investigate the spatial deployment problem for multiple drone-cells, considering the D2B link constraint. Based on the A2G pathloss model in [12] and the D2B pathloss model in [7], a framework of Drone Assisted Radio Access Networks (DA-RAN) is proposed. The user coverage and D2B backhual features of drone-cells are analyzed via stochastic method. The drone-cell deployment problem in DA-RAN is formulated to maximize the user coverage ratio when a dedicated number of drone-cells is given. Three constraints are the quality of D2B links, the maximal user number supported per drone-cell, and the multi-drone-cell interference to users. This optimization is NP-hard which can be solved by heuristic approaches. By customizing heuristic algorithms in related works into the DA-RAN scenario, a pure PSO based algorithm is proposed. To further improve the heuristic's performance, a per-Drone Iterated PSO (DI-PSO) algorithm is designed to find optimized deployments corresponding to different numbers of drone-cell respectively. Compared with the pure PSO based algorithm, the DI-PSO algorithm can achieve higher coverage ratios with less iteration times.

The remainder of this paper is organized as follows. In Section II the DA-RAN framework and the system model are presented, followed by the stochastic analyses in Section III. The drone-cell deployment problem is formulated in Section IV, with both pure PSO and DI-PSO algorithms being proposed in Section V. Numerical results are presented in Section VI. The conclusion is given in Section VII.

II. PRELIMINARIES AND SYSTEM MODEL

A. DRONE ASSISTED RADIO ACCESS NETWORKS

The framework of DA-RAN is shown in Fig. 1. Similar to the Cloud-RAN (C-RAN) architecture, drone-cells perform as aerial RRHs that connect with their corresponding BSs. For each BS in DA-RAN, a swarm of drone-cells are deployed by it over the demanding areas (DAs) where users cannot have effective connections with the BS. Two typical types of DA

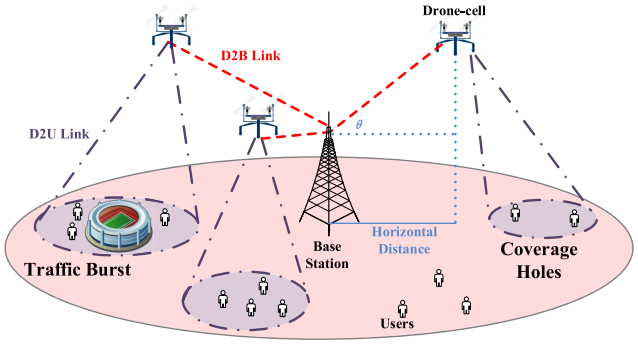

FIGURE 1. Drone assisted radio access networks.

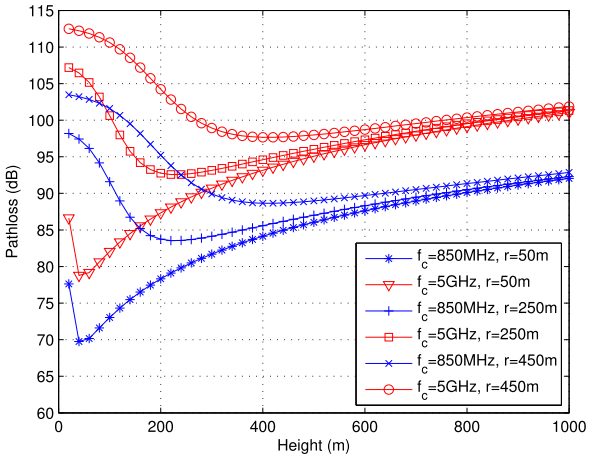

FIGURE 2. D2U pathloss model.

are Traffic Burst Spots (TBSs) and Coverage Holes (CHs). In TBSs, massive data traffic between users and the BS is generated at same time, which cannot be supported by the inadequate Resource Blocks (RBs) simultaneously. In CHs, effective user-to-BS links are blocked by obstacles, such as high buildings. Since appropriately deployed drone-cells can maintain reliable LoS U2D and D2B links, the unserved users in DAs can communicate with the BS through accessing drone-cells which act as relays. According to the spatial and temporal variations of DAs, the deployments of drone-cells can be adjusted by the BS in a flexible way, which enhances RAN's capability to cope with dynamic traffic.

The DA-RAN involves three types of links: User-to-BS (U2B) links, Drone-to-User (D2U) links and Drone-to-BS (D2B) links.

U2B links: U2B links are classic Up/Down links between users and BSs without drone-cell's involvement. In DA-RAN, U2B links co-exist with D2U and D2B links in DAs without being interfered by them. There is no effective U2B link for users in CHs, while parts of users in TBSs can access BSs via U2B links.

D2U links: D2U links connect drone-cells and users in DAs. To alleviate interference and bring additional resources for users in TBSs, the D2U links are expected to operate in different spectrum from the licensed U2B bands. Currently, the TV White Space [17], cognitive radio [18], and the WiFi bands used by commercialized drone products [19] are candidates for conducting D2U communications.

D2B links: Drone-cells communicate with corresponding BSs through D2B links. Though the LoS feature of D2B links, due to the same level of drone-cell flying heights and BS antenna heights, guarantees the reliability, the capacity of D2B links remains challenging since each D2B link has to relay all the data between the BS and users covered by the drone-cell. One promising solution for the capacity issue is the millimeter wave (mmWave) technology that can provide up to 20Gbps data-rate transmission [20]. It is appealing and feasible to employ mmWave into D2B communications due to the following reasons. First, drone-cells are expected to hover on fixed position, and maintain the quasi-static status to corresponding BSs during the interval between adjacent re-deployments. The frequent re-directing of beams can be avoided, which results in more time for effective mmWave data transmissions [21]. Second, the ideal transmission environment of mmWave technology is the LoS links, which are naturally supported by D2B communications [22]. Meanwhile, the MAC protocol of D2B links can be customized to promote performance [23]. For instance, the authentication process can be simplified to reduce latency [24].

B. DRONE-CELL LINK PATHLOSS MODELS

Impacted by the flying height and mobility of drone-cells, both D2U and D2B links in DA-RAN have the unique channel features, which cannot be appropriately modeled by the common U2B pathloss model. In this paper, state-of-the-art drone-cell link pathloss models are leveraged to analyze D2U and D2B links respectively.

The A2G pathloss model proposed in [12] is used to analyze D2U links. Based on the A2G pathloss model, the LoS probability of D2U link is [12]:

$$P_{\mathrm{LoS}}(r,h)=\frac{1}{1+a\exp(-b(\arctan(\frac{h}{r})-a))}, \tag{1}$$

where h is the drone-cell flying altitude, r is the horizontal distance between the drone-cell and the user. a and b are constant values determined by environment, such as urban, suburban, rural, etc. Neglecting the antenna heights of users and drone-cells, the average D2U pathloss can be calculated as follows [12]:

$$PL(r,h)=20\log(\frac{4\pi f_c\sqrt{h^2+r^2}}{c}) + P_{\mathrm{LoS}}(r,h)\eta_{\mathrm{LoS}}+(1-P_{\mathrm{LoS}}(r,h))\eta_{\mathrm{NLoS}}, \tag{2}$$

where f_c (in Hz) is the carrier frequency, c (in m/s) is the speed of light. η_{LoS} and η_{NLoS} are average additional losses for LoS and NLoS links which are environment-dependent. For instance, in urban environment the parameter list $(a, b, \eta_{\mathrm{LoS}}, \eta_{NLoS})$ is $(9.61, 0.16, 1, 20)$.

Fig. 2 shows the average D2U pathloss versus drone-cell altitude for different r and f_c. From Fig. 2, all pathloss

curves decrease first then increase slowly with the increasing of altitude. This is because in low altitude space, D2U pathloss is mainly determined by the LoS probability, raising altitude leads to sharp increasing of $P_{\mathrm{LoS}}(r,h)$ and decreases the pathloss level; while in high altitude space, $P_{\mathrm{LoS}}(r,h)$ remains nearly constant for all altitude values, and the pathloss curves are dominated by free space attenuation instead of $P_{\mathrm{LoS}}(r,h)$. Apart from the altitude, horizontal distance r and carrier frequency f_c also influence the D2U pathloss. Increasing r can raise all pathloss values on a curve and change the curve's shape. Increasing f_c impacts the first term in Eq. (2), and shifts the whole curve up by a constant value.

Dominated by LoS links, there is no random factor in the model of average D2B pathloss [7]. The average D2B pathloss is calculated by the cellular-to-UAV pathloss model in [7], which can be expressed as follows:

$$PL(r_{\mathrm{DB}},\theta) = 10\alpha\log(r_{\mathrm{DB}}) + A(\theta-\theta_0)\mathrm{e}^{(\frac{\theta_0-\theta}{B})} + \eta_0, \quad (3)$$

where r_{DB} is the horizontal distance between the drone-cell and the BS. θ indicates the vertical angle between the drone-cell and the BS in degree. α, A, θ_0, B, and η_0 represent the terrestrial pathloss exponent, excess pathloss scaler, angle offset, angle scaler, and excess pathloss offset, respectively. Except r_{DB} and θ, all other parameters in Eq. (3) are constants depending on different environments. For the suburban environment investigated by [7], the values of parameter list $(\alpha, A, \theta_0, B, \eta_0)$ is $(3.04, -23.29, -3.61, 4.14, 20.7)$. Since all experiments and modeling conducted in [7] use 850MHz frequency band that falls into the widely used LTE bands ranging from 700MHz to 900MHz, the carrier frequency is not reflected as one parameter in Eq. (3).

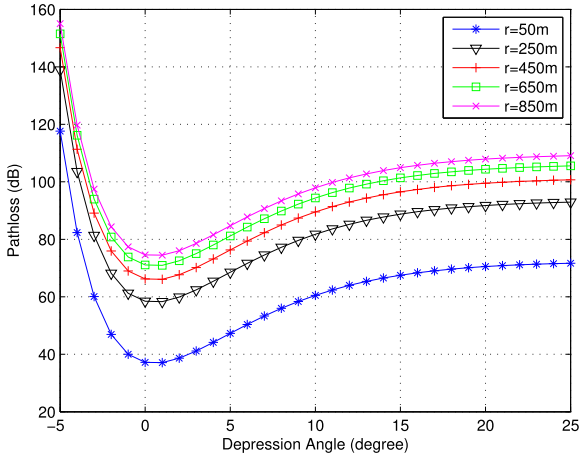

FIGURE 3. D2B pathloss model.

Curves of average D2B pathloss versus drone-cell to BS vertical angle under different r_{DB} are shown in Fig. 3. All pathloss curves decrease first then increase with the increasing of θ. The minimal pathloss values are achieved around 0° for all curves. Different from D2U links, the D2B links can keep maintaining LoS condition due to less obstacles between them, so the dominate coefficient that impacts average pathloss is the spatial distance d_{DB} between drone-cell and the BS. For any fixed r_{DB}, d_{DB} that minimizes the free space attenuation can be obtained when θ equals to 0°, which is reflected as the minimal value of the curve.

C. SYSTEM MODEL

Based on preceding drone-cell pathloss models, we investigate the 3D deployment of multiple drone-cells corresponding to one BS. Given the 3D space, the BS is fixed at the origin point (coordinate (0, 0, 0)) with ground coverage radius R_{bs}. The ground coverage area of the BS on X-Y plane $|\mathcal{A}|_{\mathrm{bs}}$ is modeled as a mesh that consists of multiple grids in square shape. The area of each grid is denoted as $|\mathcal{A}|_{\mathrm{da}}$ with the side-length of $\sqrt{|\mathcal{A}|_{\mathrm{da}}}$. By dividing $|\mathcal{A}|_{\mathrm{bs}}$ into multiple grids densely, the side-length of each grid is far smaller than R_{bs} and the drone-cell flying height h, so the average D2U pathloss of different users in one grid can be considered as equal. Without loss of generality, in this paper we normalize all D2U links within one grid to suffer the same D2U pathloss between the drone-cell and the center of the grid. Specifically, each DA is uniformed as a $20m \times 20m$ grid. Given the assumption that traffic is uniformly distributed in space and independent with each other, dedicated number of grids are randomly chosen as DAs. For an arbitrary grid, the probability of being a DA can be calculated as follows:

$$p_{\mathrm{da}} = \frac{E_{\mathrm{da}}}{N_{\mathrm{g}}}, \quad (4)$$

where E_{da} is the average DA number calculated through statistic, N_{g} is the total grid number within $|\mathcal{A}|_{\mathrm{bs}}$. Based on Eq. (4), DAs are uniformly distributed over the $|\mathcal{A}|_{\mathrm{bs}}$. We assume that DAs change their size and location with a low frequency, so each drone-cell deployment can treat the random distributed DAs as a quasi-static scenario where no spatial change occurs during the interval between adjacent re-deployments. Based on the current snapshot of DAs distribution, the BS deploys drone-cells over DAs to maximize user coverage, and re-deploys them when the DAs distribution changes.

III. THEORETICAL ANALYSES

In this part we analyze the user coverage and working zone of drone-cells in DA-RAN. The main notations used in the analyses are summarized in Table. 1.

A. DRONE-CELL USER COVERAGE ANALYSIS

Without loss of generality, we assume that the user distribution follows a 2D Poisson Point Process (PPP) over the $|\mathcal{A}|_{\mathrm{bs}}$ with a user density λ. Due to the independence of each PPP point, the number of user locating in an arbitrary DA u_{da} follows a Poisson distribution:

$$P(u_{\mathrm{da}}) = \frac{(\lambda|\mathcal{A}|_{\mathrm{da}})^{u_{\mathrm{da}}}}{u_{\mathrm{da}}!}\mathrm{e}^{-\lambda|\mathcal{A}|_{\mathrm{da}}}. \quad (5)$$

TABLE 1. Summary of main notations.

Notations	Descriptions
h	flying height of the drone-cell
r	horizontal distance between one drone-cell and one DA
$\|\mathcal{A}\|_{\text{bs}}$	coverage area of the BS on X-Y plane
R_{bs}	coverage radius of the BS
$\|\mathcal{A}\|_{\text{da}}$	area of each grid
p_{da}	probability of being a DA for an arbitrary grid
N_{g}	total grid number within the BS coverage
λ	user density
u_{da}	number of user locating in an arbitrary DA
$R_{\text{dc}}(h)$	effective coverage radius of one drone-cell at height h
ξ_{LoS}	D2U LoS probability threshold
γ_{DU}	D2U free space pathloss threshold
$D_{\text{dc}}(h)$	average DA number covered by one drone-cell at height h
$U_{\text{dc}}(h)$	average user number covered by one drone-cell at height h
$\mathbb{U}_{\text{Udc}}(h)$	upper bound of $U_{\text{dc}}(h)$
$\mathbb{L}_{\text{Udc}}(h)$	lower bound of $U_{\text{dc}}(h)$
H_{opt}	optimal drone-cell height for maximizing $U_{\text{dc}}(h)$
r_{DB}	horizontal distance between drone-cell and the BS
N_{dc}	number of drone-cells
N_{da}	number of DAs
C_{dc}	Capacity of one drone-cell
R	minimal data rate required by each user
γ_{DB}	D2B pathloss threshold
N_{Imax}	maximal multi-drone-cell interference suffered by one DA

Since NLoS D2U links are not capable of supporting effective data transmissions in reality, the effective coverage radius of the drone-cell R_{dc} cannot be determined by directly using Eq. (2) with NLoS links. By constraining both LoS probability and free space pathloss, the refined drone-cell coverage constraint is expressed as:

$$\begin{cases} P_{\text{LoS}}(r,h) > \xi_{\text{LoS}} \\ \frac{4\pi f_c\sqrt{h^2+r^2}}{c} < \gamma_{\text{DU}} \end{cases} \tag{6}$$

Since the $P_{\text{LoS}}(r,h)$ is a decreasing functions of r while the free space pathloss function is an increasing functions of r, the function with a minor return value determines R_{dc}. For a fixed height h, R_{dc} can be expressed as a function of h through rewriting Eq. (6) :

$$R_{\text{dc}}(h) = \min\Big(\frac{h}{\tan(a-\frac{1}{b}\ln\frac{1-\xi_{\text{LoS}}}{a\xi_{\text{LoS}}})}, \sqrt{(\frac{c\gamma_{\text{DU}}}{4\pi f_c})^2 - h^2}\Big), \tag{7}$$

where the the min function returns the minor one of its two items, the former reflects the LoS probability constraint, while the later represents the free space pathloss constraint. Given $R_{\text{dc}}(h)$ and p_{da}, the average number of DAs covered by one drone-cell flying at height h can be calculated as:

$$D_{\text{dc}}(h) = p_{\text{da}}N_{\text{g}}\frac{|\mathcal{A}|_{\text{da}}}{|\mathcal{A}|_{\text{bs}}} = p_{\text{da}}N_{\text{g}}\frac{R_{\text{dc}}^2(h)}{R_{\text{bs}}^2}. \tag{8}$$

In following analyses, we use R_{dc} and D_{dc} to represent the returns of $R_{\text{dc}}(h)$ and $D_{\text{dc}}(h)$ for a given h, respectively.

Assume that k DAs occurs in the $|\mathcal{A}|_{\text{da}}$ of an arbitrary drone-cell. Based on Eq. (5), u_{dc} users can be covered by the drone-cell with the probability of:

$$P(u_{\text{dc}}) = \frac{(\sum_{i=0}^{k} p_i\lambda|\mathcal{A}|_{\text{da}})^{u_{\text{dc}}}}{u_{\text{dc}}!}\text{e}^{-\sum_{i=0}^{k} p_i\lambda|\mathcal{A}|_{\text{da}}}, \tag{9}$$

where p_i indicates the LoS link probability between DA i and the drone-cell, which is calculated by Eq. (1). $p_i\lambda$ represents the number of users effectively covered by the drone-cell in DA i.

According to the attributes of Poisson distribution, the average number of users covered by the drone-cell $\text{E}(u_{\text{dc}})$ is:

$$\text{E}(u_{\text{dc}}) = \sum_{i=0}^{k} p_i\lambda|\mathcal{A}|_{\text{da}}. \tag{10}$$

Since the values of p_i are affected by the horizontal and vertical distances between DA i and the drone-cell, even for a given flying height h and the corresponding R_{dc}, p_is of different DAs vary. On the other hand, k in Eq. (10) is a random variable whose distribution is impacted by R_{dc}. Therefore, we have the following Proposition 1.

Proposition 1: Given the drone-cell flying at height h, the average number of effectively covered users U_{dc} can be calculated as follows:

$$U_{\text{dc}}(h) = \int_0^{R_{\text{dc}}} \frac{2r\lambda|\mathcal{A}|_{\text{da}}p_{\text{da}}N_{\text{g}}}{R_{\text{bs}}^2(1+a\exp(-b(\arctan(\frac{h}{r})-a)))}\,\text{d}r. \tag{11}$$

Proof: [Proof] Because the value of p_i is determined by the location of DA i for given h, p_i turns to be an i.i.d random variable for all DAs. Given the fact that p_i and k are independent, we have:

$$\begin{aligned} U_{\text{dc}}(h) &= \text{E}(u_{\text{dc}}) = \text{E}(p_i\lambda|\mathcal{A}|_{\text{da}})\text{E}(k) \\ &= \text{E}(p_i\lambda|\mathcal{A}|_{\text{da}})p_{\text{da}}N_{\text{g}}\frac{R_{\text{dc}}^2}{R_{\text{bs}}^2}. \end{aligned} \tag{12}$$

In Eq. (12), the expectation of k equals to the average number of DAs covered by one drone-cell D_{dc} calculated through Eq. (8). The remaining task is calculating $\text{E}(p_i\lambda|\mathcal{A}|_{\text{da}})$. For the fixed h, p_i can be treated as a function of r, and its PDF is dominated by r's distribution. Leveraging the geometric features of r, the PDF of r can be expressed as follows:

$$P(r) = \frac{\text{d}C(r)}{\text{d}r} = \frac{\text{d}}{\text{d}r}(\frac{\pi r^2}{\pi R_{\text{dc}}^2}) = \frac{2r}{R_{\text{dc}}^2} \quad r\in[0,R_{\text{dc}}], \tag{13}$$

where $C(r)$ is the CDF of r. Based on Eq. (13), the $\text{E}(p_i\lambda|\mathcal{A}|_{\text{da}})$ is calculated:

$$\begin{aligned} &\text{E}(p_i\lambda|\mathcal{A}|_{\text{da}}) \\ &= \lambda|\mathcal{A}|_{\text{da}}\text{E}(p_i(r)) \\ &= \lambda|\mathcal{A}|_{\text{da}}\int_0^{R_{\text{dc}}} \frac{1}{1+a\exp(-b(\arctan(\frac{h}{r})-a)}P(r)\,\text{d}r \\ &= \int_0^{R_{\text{dc}}} \frac{2\lambda|\mathcal{A}|_{\text{da}}r}{R_{\text{dc}}^2(1+a\exp(-b(\arctan(\frac{h}{r})-a))}\,\text{d}r. \end{aligned} \tag{14}$$

With both $\text{E}(p_i\lambda|\mathcal{A}|_{\text{da}})$ and $\text{E}(k)$ being derived, the expression of $U_{\text{dc}}(h)$ can be obtained through substituting Eq. (14)

into Eq. (12):

$$U_{\rm dc}(h) = p_{\rm da}N_{\rm g}\frac{R_{\rm dc}^2}{R_{\rm bs}^2} \times \int_0^{R_{\rm dc}} \frac{2\lambda|\mathcal{A}|_{\rm da}r}{R_{\rm dc}^2(1+a\exp(-b(\arctan(\frac{h}{r})-a)))}\,{\rm d}r = \int_0^{R_{\rm dc}} \frac{2r\lambda|\mathcal{A}|_{\rm da}p_{\rm da}N_{\rm g}}{R_{\rm bs}^2(1+a\exp(-b(\arctan(\frac{h}{r})-a)))}\,{\rm d}r. \quad (15)$$

Proposition 1 has been proven. ■

Though $U_{\rm dc}(h)$ can be expressed as a function of h with an integral of r included, the close-form of $U_{\rm dc}(h)$ is hard to be derived due to hyper-geometric functions are involved after calculating the integral. However, we can still analyze the upper and lower bounds of $U_{\rm dc}(h)$ through fixing the $P_{\rm LoS}(r,h)$ of each DA as 1 and the smallest available $P_{\rm LoS}(r,h)$ which is achieved at the coverage boundary of $R_{\rm dc}$, respectively. In this way, the integral of r can be removed from both upper and lower bound expressions of $U_{\rm dc}(h)$. Specifically, the upper bound of $U_{\rm dc}(h)$ is:

$$\mathbb{U}_{\rm Udc}(h) = \lambda|\mathcal{A}|_{\rm da}p_{\rm da}N_{\rm g}\frac{R_{\rm dc}^2}{R_{\rm bs}^2}, \quad (16)$$

and the lower bound is:

$$\mathbb{L}_{\rm Udc}(h) = \frac{\lambda|\mathcal{A}|_{\rm da}}{1+a\exp(-b(\arctan(\frac{h}{R_{\rm dc}})-a))}p_{\rm da}N_{\rm g}\frac{R_{\rm dc}^2}{R_{\rm bs}^2} = \frac{\lambda|\mathcal{A}|_{\rm da}p_{\rm da}N_{\rm g}R_{\rm dc}^2}{R_{\rm bs}^2(1+a\exp(-b(\arctan(\frac{h}{R_{\rm dc}})-a)))}. \quad (17)$$

According to Eq. (7), $R_{\rm dc}$ is determined by the minimal value of one increasing function of h and one decreasing function of h. The maximal $R_{\rm dc}$ can be obtained at the intersection point of two functions, let:

$$\frac{H_{\rm opt}}{\tan(a-\frac{1}{b}\ln\frac{1-\xi_{\rm LoS}}{a\xi_{\rm LoS}})} = \sqrt{(\frac{c\gamma_{\rm DU}}{4\pi f_c})^2 - H_{\rm opt}^2}, \quad (18)$$

the optimal height $H_{\rm opt}$ equals to:

$$H_{\rm opt} = \frac{\tan(a-\frac{1}{b}\ln\frac{1-\xi_{\rm LoS}}{a\xi_{\rm LoS}})\frac{c\gamma_{\rm DU}}{4\pi f_c}}{\sqrt{1+\tan(a-\frac{1}{b}\ln\frac{1-\xi_{\rm LoS}}{a\xi_{\rm LoS}})}}. \quad (19)$$

Based on preceding analyses, we have the Corollary 1 of Proposition 1.

Corollary 1: Given the drone-cell flying height h, the upper bound of the average user number $U_{\rm dc}(h)$ efficiently covered by the drone-cell is the function of h, and obtains its maximum when h equals to $H_{\rm opt}$.

B. DRONE-CELL WORKING ZONE ANALYSIS

To maintain the qualities of D2B links, a working zone in which drone-cell can maintain the D2B pathloss smaller than a given threshold $\gamma_{\rm DB}$ has to be identified. However, since the D2B pathloss model is a function of $r_{\rm DB}$ and θ, the available working zone of drone-cell in the 3D space cannot be estimated intuitively. In this section, we transform θ into a function of h and $r_{\rm DB}$ to represent the working zone.

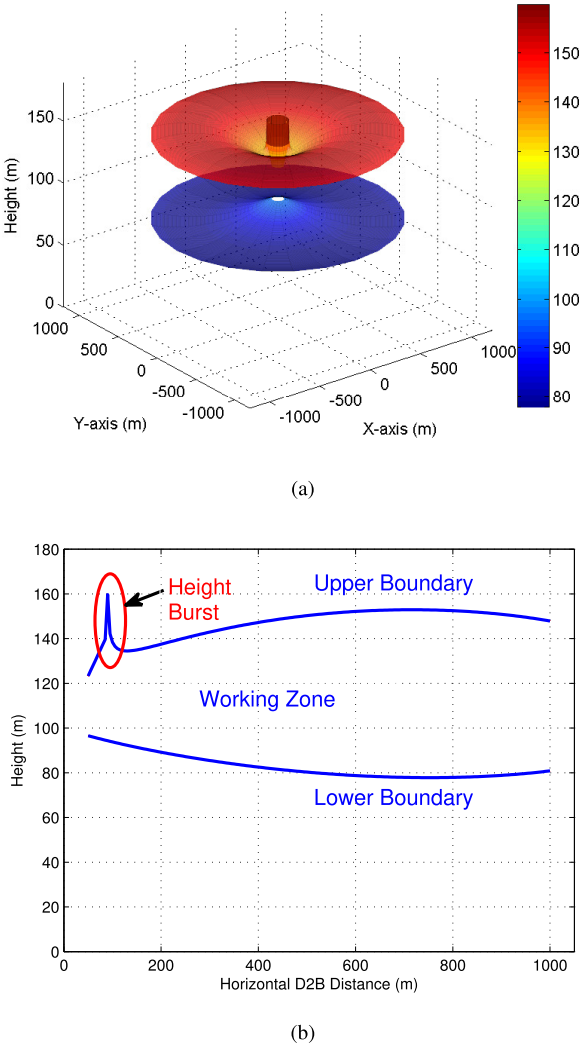

FIGURE 4. Drone-cell working zone, a) 3D view, b) 2D projection on X-Z plane.

Fig. 4 shows an example of the drone-cell working zone in both 3D and side views. The BS in Fig. 4 is configured with the height of $100m$ and $R_{\rm bs} = 1000m$, and $\gamma_{\rm DB}$ is set as $80dB$. According to Fig. 4, the drone-cell working zone is constrained by a torus shape hovering around the top of BS horizontally. By increasing $r_{\rm DB}$, the difference of the upper and lower height boundaries increases first, then decreases slowly. The maximal difference is achieved around $r_{\rm DB} = 700m$ with the available drone-cell height ranging from $80m$ to $150m$. The torus shape of drone-cell working zone can be explained as follows. According to Fig. 3, given a fixed pathloss threshold, the available θ range is reduced with the increasing of $r_{\rm DB}$. The corresponding h_θ for each θ is calculated as:

$$h_\theta = r_{\rm DB}\tan(\theta) + H_{\rm bs}, \quad (20)$$

whose absolute value rises with r_{DB}'s increasing as long as θ is fallen into the available range. For a small r_{DB}, the reducing level of θ range is compensated by the increasing of h_θ, so the working zone height range are extending by increasing r_{DB}. While for a large r_{DB}, the increasing of h_θ cannot make up the serious reduction of θ range, and the working zone height range turns to shrink when r_{DB} keeps increasing.

One interesting effect observed from Fig. 4 is the sharp height burst of the working zone that is close to the BS. From Fig. 3, we notice that for a small r_{DB}, the pathloss curve can converge to a value less than the threshold when height increases to infinity, such as the curve corresponding to $r_{\mathrm{DB}} = 50m$. Without a θ to constraining the upper boundary, the available height at such r_{DB} can reach a large value until being limited by the large-scale pathloss term in Eq. (3). However, as long as r_{DB} rises to certain value whose corresponding pathloss curve reaches higher than the threshold, the upper boundary of height range is back to normal with the constraint of θ. Though this height burst provide additional space for drone-cell deploying, its usage is still relatively limited in reality due to the narrow range.

IV. PROBLEM FORMULATION

Based on the preceding analyses, we formulate the 3D drone-cell deployment problem in this section.

Considering a quasi-static DAs scenario between adjacent re-deployments, N_{da} grids are selected as DAs. A boolean parameter ϵ_i is defined to show the coverage state of the ith DA ($0 \le i \le N_{\mathrm{da}}$):

$$\epsilon_i = \begin{cases} 1 & \text{if DA } i \text{ is covered by a drone-cell,} \\ 0 & \text{if DA } i \text{ is uncovered.} \end{cases} \tag{21}$$

By defining ϵ_i, the purpose of enhancing user coverage can be translated to the objective of maximizing the summation of ϵ_i through deploying drone-cells in appropriate positions. Assuming the BS release N_{dc} number of drone-cells, the pathloss between drone-cell j ($0 \le j \le N_{\mathrm{dc}}$) and DA i is constrained by Eq. (6). Defining that DA i can be effectively covered by drone-cell j, as long as the D2U pathloss between them is less than threshold γ_{DU}. Since that, Eq. (21) can be updated as follows:

$$\epsilon_{ij} = \begin{cases} 1 & \text{if Eq. (6) holds,} \\ 0 & \text{else,} \end{cases} \tag{22}$$

where h_j is drone-cell j's hovering height, r_{ij} is the horizontal distance between drone-cell j and DA j.

Three constraints are considered in the deployment problem. First, the maximum number of users served by one drone-cell is defined as:

$$M_u = \lfloor \frac{C_{\mathrm{dc}}}{R} \rfloor, \tag{23}$$

where R is minimal data rate required by each user, and C_{dc} is the capacity of one drone-cell. To simplify the analysis, we assume that both R and C_{dc} are the same for arbitrary user and drone-cell respectively. Leveraging the average number of effective users in one DA calculated by Eq. (14), Eq. (23) can be transformed to express the maximal DA number that can be supported by one drone-cell:

$$C_{\mathrm{da}} = \lfloor \frac{C_{\mathrm{dc}}}{\mathrm{E}(p_i \lambda |\mathcal{A}|_{\mathrm{da}}) R} \rfloor, \tag{24}$$

The second constraint is maintaining the qualities for every D2B links. Defining a pathloss threshold γ_{DB}, we argue that any drone-cells being deployed must guarantee that their average D2B pathloss level $PL(r_{jb}, \theta_{jb})$ is less than γ_{DB}, where r_{jb} is the horizontal distance between drone-cell j and the BS, and θ_{jb} represents the vertical angle between drone-cell j and the antenna of BS. This constraint sets the working zone in which drone-cells choose their optimal deploying positions.

Multi-drone-cell interference is considered as the third constraint. Noticing that all D2U communications are carried by the same spectrum band, one user can only be allocated to one drone-cell. When one DA is served by two or more drone-cells simultaneously, the users in such DA can suffer serious interference from redundant drone-cell, which is defined as multi-drone-cell interference. To prevent this issue, we use I_i as the indicator of multi-drone-cell interference suffered by DA i:

$$I_i = \max\{\sum_{j=1}^{N_{\mathrm{dc}}} \epsilon_{ij} - 1, 0\}. \tag{25}$$

When DA i is uncovered or covered by only one drone-cell, I_i equals to 0; otherwise I_i equals to the number of interfering drone-cells. By defining a maximal allowed I_i value, the overlapping of different drone-cell coverages can be minimized effectively.

Finally, the 3D drone-cell deployment problem is formulated as the following optimization problem to maximize $\mathcal{U}$, i.e., the number of DAs being covered:

$$\begin{aligned} \max_{x_j, y_j, h_j} \quad & \mathcal{U} = \sum_{j=1}^{N_{\mathrm{dc}}} \sum_{i=1}^{N_{\mathrm{da}}} \epsilon_{ij} - \sum_{i=1}^{N_{\mathrm{da}}} I_i \\ s.t. \quad & \sum_{i=1}^{N_{\mathrm{da}}} \epsilon_{ij} \le \lfloor \frac{C_{\mathrm{dc}}}{\mathrm{E}(p_i \lambda |\mathcal{A}|_{\mathrm{da}}) R} \rfloor \\ & PL(r_{jb}, \theta_{jb}) < \gamma_{\mathrm{DB}} \\ & I_i \le N_{\mathrm{Imax}}, \end{aligned} \tag{26}$$

where (x_j, y_j, h_j) is the coordinate of drone-cell j being deployed at. N_{Imax} indicates the maximum allowed interference level suffered by one DA. Note that the constraints 1 and 2 are applying for each drone-cell j, while the constraint 3 is examined for every DA i.

V. PER-DRONE ITERATED PSO ALGORITHM

Similar to the classic BS location planning problem [25], the 3D drone-cell deployment problem in Eq. (26) is also recognized as NP-hard [16]. Due to the heterogeneous pathloss models for D2U and D2B links in 3D space, the optimal

solution is hard to reach through mathematical deductions. So heuristic algorithms, especially the evolutionary heuristics such as Genetic Algorithm (GA), PSO, etc., are considered as alternative choices to approaching the optima.

PSO algorithm is employed by both [16] and [25] to solve similar drone-cell coverage problems. Compared with other heuristics (e.g., GA), PSO has following advantages: 1) fewer numerical parameters are required which simplifies the implementation; 2) lower computational cost and faster convergence speed can be achieved [26]; 3) PSO can deal with an infinite set of drone-cell combinations unlike other algorithms (e.g., GA) that require a finite set of drone-cell combinations to be executed [25]. which is suitable for drone-cell deployment scenario where re-deployment speed matters.

Algorithm 1 Pure PSO Based Algorithm for Drone-Cell Deployment in DA-RAN

1: Define a particle chosen space $\mathcal{S}$ as same as the drone-cell working zone corresponding to γ_{DB}.
2: Generate L random particles in $\mathcal{S}$ as initial population. For each initial particle $\mathbf{W}^{(l)}(0)$,$l = 1, \ldots, L$, it is expressed as a random vector with size N_{dc}.
3: Re-generate the invalid elements in each $\mathbf{W}^{(l)}(0)$ vector until they meet constraint 1 and 3 in Eq. (26) simultaneously. Randomly generate initial velocity vector $\mathbf{V}^{(l)}(0)$ for each particle.
4: Calculate $U^{(l)}(0)$ through Eq. (26) for each $\mathbf{W}^{(l)}(0)$. Set $U^{(global)} = \max\{U^{(l)}(0), l = 1, \ldots, L\}$, $\mathbf{W}^{(global)} = \mathbf{W}^{(l)}(0)$ which achieves the $U^{(global)}$. Set $U^{(l,local)} = U^{(l)}(0)$, $\mathbf{W}^{(l,local)} = \mathbf{W}^{(l)}(0)$. Define maximum iteration number M_{Ite}.
5: **for** $t = 1, \ldots, M_{Ite}$ **do**
6: **for** $l = 1, \ldots, L$ **do**
7: Calculate $\mathbf{W}^{(l)}(t)$.
8: **while** $\mathbf{W}^{(l)}(t)$ exceeds any Eq. (26) constraints **do**
9: Re-generate the invalid elements in $\mathbf{W}^{(l)}(t)$.
10: **end while**
11: Calculate $U^{(l)}(t)$,$\mathbf{V}^{(l)}(t)$.
12: **if** $U^{(l)}(t) > U^{(l,local)}$ **then**
13: $U^{(l,local)} = U^{(l)}(t)$, $\mathbf{W}^{(l,local)} = \mathbf{W}^{(l)}(t)$.
14: **end if**
15: **if** $U^{(l,local)} > U^{(global)}$ **then**
16: $U^{(global)} = U^{(l,local)}$, $\mathbf{W}^{(global)} = \mathbf{W}^{(l,local)}$.
17: **end if**
18: **end for**
19: **end for**

We customize the PSO algorithms proposed in [16] and [25] to form a pure PSO based algorithm, which is shown in Algorithm 1. Compared to the PSO algorithms in [16] and [25], the pure PSO algorithm involves the D2B link constraint specified in the DA-RAN scenario. In the pure PSO algorithm, the velocity vector of particle l at iteration t is defined as follows:

$$\begin{aligned}\mathbf{V}^{(l)}(t) = {} & \phi\mathbf{V}^{(l)}(t-1) \\ & + c_1\phi_1(\mathbf{W}^{(l,local)}(t-1) - \mathbf{W}^{(l)}(t-1)) \\ & + c_2\phi_2(\mathbf{W}^{(global)}(t-1) - \mathbf{W}^{(l)}(t-1)), \quad (27)\end{aligned}$$

where ϕ is the inertia weight that determines convergence speed. c_1 and c_2 are personal and global learning coefficients respectively. ϕ_1 and ϕ_2 are positive random variables. With the $\mathbf{V}^{(l)}(t)$ obtained from Eq. (27), $W^{(l)}(t)$ is updated as:

$$\mathbf{W}^{(l)}(t) = \mathbf{W}^{(l)}(t-1) + \mathbf{V}^{(l)}(t). \quad (28)$$

The pure PSO based algorithm treats the combination of N_{dc} drone-cell positions as one particle represented in vector form, which brings additional dependency between drone-cells. Since $\mathbf{W}^{(l)}(t)$'s elements (each drone-cell position) are dependent with each other during iteration, the diversity of the particle searching space is seriously reduced. Though relatively less computational cost and shorter convergence time can be obtained in this way, the probability of falling into local optima increases. To compensate this, number pf particle and iteration times have to be added, which increases the complexity and total cost. Besides, the vector formed $\mathbf{W}^{(l)}(t)$ is hard to be re-generated to ensure that all elements fits Eq. (26)'s constraints simultaneously, especially the interference constraint which only allows the adjustments of partial elements. As a result, redundant re-generations must be executed before randomly generating a suitable particle.

To alleviate the aforementioned issues of pure PSO based algorithm, we propose the DI-PSO algorithm which employs the PSO algorithm independently on each drone-cell. The detail of DI-PSO is given in Algorithm 2. In DI-PSO, the particles are no longer vectors but individual positions. Due to the different particle structures, the updating functions of particle velocity and position are revised as follows:

$$\begin{aligned}V_d^{(l)}(t) = {} & \phi V_d^{(l)}(t-1) \\ & + c_1\phi_1(W_d^{(l,local)}(t-1) - W_d^{(l)}(t-1)) \\ & + c_2\phi_2(W_d^{(global)}(t-1) - W_d^{(l)}(t-1)), \quad (29)\end{aligned}$$

and

$$W_d^{(l)}(t) = W_d^{(l)}(t-1) + V_d^{(l)}(t). \quad (30)$$

For each drone-cell d, PSO algorithm is used to calculate its best deployed position in which the maximal number of covered DAs is achieved. With each drone-cell being independently deployed, the spatial ergodicity of DI-PSO is increased which leads to higher probability of finding the global optima. meanwhile, the set of DAs to be covered by drone-cell d ($\mathbf{A}(d)$) is updated by each drone-cell iteration with only uncovered DAs remaining in it. This mechanism can reduce the times of re-generating $W_d^{(l)}(t)$ through prevent inter-drone-cells interference in a proactive way.

Algorithm 2 DI-PSO algorithm for drone-cell deployment in DA-RAN

Define a particle chosen space $\mathcal{S}$ as same as the drone-cell working zone corresponding to γ_{DB}.
Initiate uncovered DAs set $\mathbf{A}(1)$ contains all DAs.
for $d = 1, \ldots, N_{\mathrm{dc}}$ **do**
  Generate L random particles $W_d^{(l)}(0)(l = 1, \ldots, L)$ as initial population of drone-cell d within $\mathcal{S}$.
  Re-generate the invalid $W_d^{(l)}(0)$ until they meet constraint 1 and 3 in Eq. (26) simultaneously. Randomly generate initial velocity $V_d^{(l)}(0)$ for each $W_d^{(l)}(0)$.
  Calculate $U_d^{(l)}(0)$ with input $\mathbf{A}(d)$. Set $U_d^{(global)} = \max\{U_d^{(l)}(0), l = 1, \ldots, L\}$, $W_d^{(global)} = W_d^{(l)}(0)$ which achieves the $U_d^{(global)}$. Set $U_d^{(l,local)} = U_d^{(l)}(0)$, $W_d^{(l,local)} = W_d^{(l)}(0)$.
  for $t = 1, \ldots, M_{Ite}$ **do**
    for $l = 1, \ldots, L$ **do**
      Calculate $W_d^{(l)}(t)$.
      while $W_d^{(l)}(t)$ exceeds Eq. (26) constraints **do**
        Re-generate $W_d^{(l)}(t)$.
      end while
      Calculate $U_d^{(l)}(t)$,$V_d^{(l)}(t)$.
      if $U_d^{(l)}(t) > U_d^{(l,local)}$ **then**
        $U_d^{(l,local)} = U_d^{(l)}(t)$, $W_d^{(l,local)} = W_d^{(l)}(t)$.
      end if
      if $U_d^{(l,local)} > U_d^{(global)}$ **then**
        $U_d^{(global)} = U_d^{(l,local)}$,
        $W_d^{(global)} = W_d^{(l,local)}$.
      end if
    end for
  end for
  Calculate $\mathbf{A}_{new}(d)$ as the set of DAs newly covered by drone-cell d.
  Update $\mathbf{A}(d+1) = \mathbf{A}(d) - \mathbf{A}_{new}(d)$.
end for

TABLE 2. Simulation parameters.

Simulation Parameters	Numerical Values
BS coverage radius R_{bs}	900m
DA size	20m×20m
$(a, b, \eta_{\mathrm{LoS}}, \eta_{NLoS})$	(4.88,0.43,0.1,21)
(D2U f_c, D2B f_c)	(2.4GHz, 850MHz)
(γ_{DU}, γ_{DB}(normalized in dB))	(89dB, 80dB)
λ	0.025 person/m^2
C_{dc}	1Gbps
R	100Mbps
N_{Imax}	2
Particle population	400
Maximum number of iteration	50

VI. NUMERICAL RESULTS

Simulations are conducted to compare the performance of both proposed algorithms. Considering the single BS with 900m coverage radius in a suburban scenario, the simulation parameters are listed in Table. 2. 2.4GHz WiFi band is chosen as the carrier f_c for its wide adoption in previous works and commercial drone products [19], [27]. The 850MHz LTE band are used to support D2B communications. To suit the scenario where the D2B pathloss model is built, propagation parameters for suburban are chosen. Allocating different bands to D2U and D2B links also prevent the interference between them. Both γ_{DU} and γ_{DB} are set within the range used by related works [15].

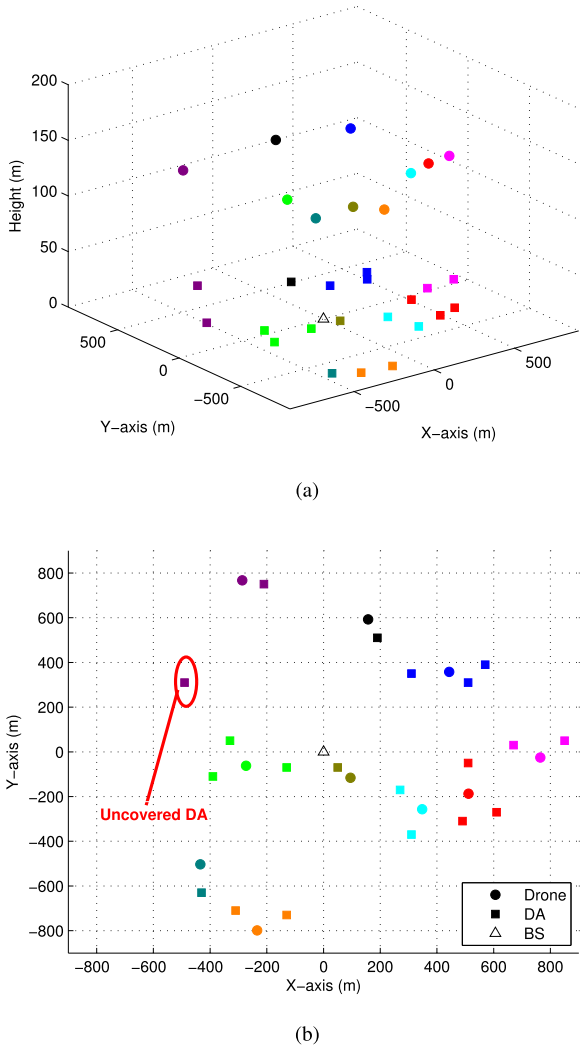

FIGURE 5. Drone-cell deployment example generated by DI-PSO algorithm, a) 3D view, b) 2D projection on X-Y plane.

Fig. 5 shows one example drone-cell deployment generated by the DI-PSO algorithm. N_{da} is 20 and N_{dc} equals 10 in this scenario. Triangle dot locating at the origin of coordinate represents the BS. DAs are indicated as square dots and drone-cells are illustrated as circle dots. DAs covered by the same drone-cell are with the same color as the drone-cell's. In this example, 19 out of 20 DAs are covered by drone-cells with only one uncovered DA that locates near the edge of the BS coverage. Since all drone-cells have to guarantee D2U and D2B pathloss less than γ_{DU} and γ_{DB} simultaneously, the marginal location of the uncovered DA

implies no drone-cell can be allocated for it without breaking pathloss constraints. The label of each drone-cell in Fig. 5 represents its iteration order d in DI-PSO algorithm. The first deployed drone-cell is allocated with 3 DAs, while the fifth to tenth drone-cells can only occupy 1 DA by each. This trend is caused by updating $\mathbf{A}(d)$ per-iteration with only uncovered DAs being left, which can be regarded as one kind of greedy mechanism to find the corresponding maximal coverage for any given N_{dc}.

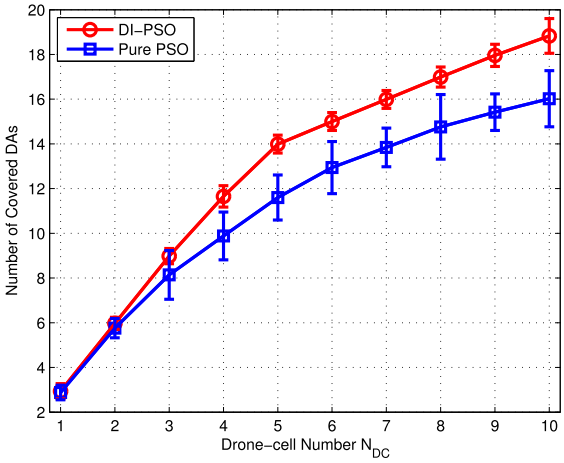

FIGURE 6. Coverage comparison between pure PSO and DI-PSO algorithms with different number of drone-cells.

Fig. 6 shows the number of effectively covered DAs versus the available drone-cell number N_{dc} for both algorithms. Using the same DAs scenario shown in Fig. 5, simulations are conducted 100 times for each algorithm under each drone-cell number. Noting that the error-bars attached on each curve indicate the standard deviation level of their corresponding test points. As shown in Fig. 6, two algorithms are comparable when N_{dc} equals to 1 or 2. By increasing N_{dc}, both curves keep increasing while the DI-PSO always maintains average 2 more DAs being covered comparing with pure PSO. This poor performance of pure PSO algorithm is caused by the limited diversity of particle searching space. The increasing trends of two curves are all dented when N_{dc} reaches large values, while the pure PSO curve increases slower with average 3 covered DAs being exceeded by DI-PSO curve when $N_{\mathrm{dc}} = 10$. Besides, little variance is achieved by DI-PSO algorithm for each N_{dc}, which indicates DI-PSO's stability of converging to optimized results.

Fig. 7 compares the coverage ratios of the two algorithms for the DA number of 20, 50 and 100, respectively. The coverage ratio is defined as the number of covered DAs over the total number of DAs. The number of available drone-cells N_{dc} is fixed as 10. For each DAs number, 100 snapshots of DA distribution are generated to run Monte Carlo tests. As Fig. 7 indicates, coverage ratios of both algorithms are decreased by increasing the number of DAs. Since a larger number of DAs leading to higher DA density within the fixed BS coverage area, the serious inter-drone-cell interference caused by the

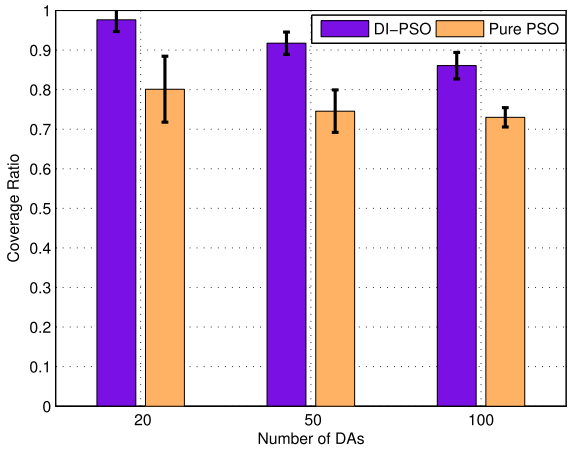

FIGURE 7. Coverage comparison between pure PSO and DI-PSO algorithms with different numbers of DAs.

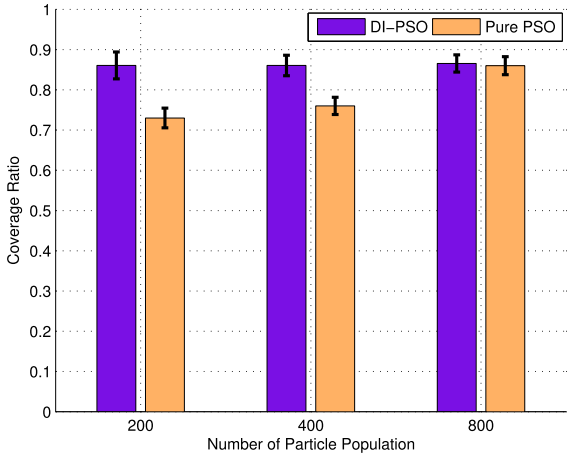

FIGURE 8. Performance comparison between pure PSO and DI-PSO algorithms with different particle populations.

high DA density is the main reason for the decrease of the coverage ratio. Comparing with the pure PSO algorithm, the DI-PSO algorithm achieves higher coverage ratios with less variances in all scenarios. Note that the performance of pure PSO based algorithm in both Fig. 6 and Fig. 7 is better than the similar simulation in [28]. This performance increase is caused by applying new D2B pathloss model to generate the working zone which constrains the particle searching space for the pure PSO based algorithm. The number of particle re-generations is also reduced by applying the working zone at the beginning of the algorithm.

To test the impacts of the limited particle searching space in pure PSO. We further compare the performance of two algorithms with the particle population set as 200, 400, and 800. The 100 snapshots of DA distribution with 100 DAs are used for testing. Fig. 13 shows the simulation results. For DI-PSO, its coverage ratios under different particle populations remains no change, with only the standard deviation decreases by increasing the particle population. This result indicates that the DI-PSO can effectively converge to the

optimal solution with a small particle population. For pure PSO based algorithm, its coverage ratio keeps rising with the increasing particle population, and reaches the same level when the particle population equals to 800. However, the coverage ratio achieved by pure PSO with 800 particle population size can be reached by DI-PSO with only 200 particle population size, which proves that the DI-PSO is more efficient than the pure PSO based algorithm in terms of computation costs.

VII. CONCLUSION

In this paper, we have theoretically analyzed the drone-cell user coverage and feasible working zone by leveraging the emerging D2U and D2B pathloss models. The 3D deployment problem of drone-cell in DA-RAN has been formulated to maximize the user coverage while maintaining D2B link qualities, which is solved by the DI-PSO heuristic solution. With drone-cells' capabilities of providing LoS links and enabling dynamic deployments, the results from this research can shed light on the DA-RAN research. In addition, the drone-cell user coverage and working zone analysis results offer general understandings to inspire future research concerning the drone-cell coverage. For our future work, we will explore the drone-cell path-planning and scheduling problems constrained by the energy capacity of drone-cells.

REFERENCES

[1] I. Bor-Yaliniz and H. Yanikomeroglu, "The new frontier in ran heterogeneity: Multi-tier drone-cells," *IEEE Commun. Mag.*, vol. 54, no. 11, pp. 48–55, Nov. 2016.
[2] N. Zhang, S. Zhang, P. Yang, O. Alhussein, W. Zhuang, and X. Shen, "Software defined space-air-ground integrated vehicular networks: Challenges and solutions," *IEEE Commun. Mag.*, vol. 55, no. 7, pp. 101–109, Jul. 2017.
[3] Q. Wu, Y. Zeng, and R. Zhang. (May 2017). "Joint trajectory and communication design for multi-UAV enabled wireless networks." [Online]. Available: https://arxiv.org/abs/1705.02723
[4] N. H. Motlagh, T. Taleb, and O. Arouk, "Low-altitude unmanned aerial vehicles-based Internet of Things services: Comprehensive survey and future perspectives," *IEEE Internet Things J.*, vol. 3, no. 6, pp. 899–922, Dec. 2016.
[5] Y. Zeng, R. Zhang, and T. J. Lim, "Wireless communications with unmanned aerial vehicles: Opportunities and challenges," *IEEE Commun. Mag.*, vol. 54, no. 5, pp. 36–42, May 2016.
[6] L. Gupta, R. Jain, and G. Vaszkun, "Survey of important issues in UAV communication networks," *IEEE Commun. Surv. Tuts.*, vol. 18, no. 2, pp. 1123–1152, 2nd Quart., 2016.
[7] A. Al-Hourani and K. Gomez, "Modeling cellular-to-UAV path-loss for suburban environments," *IEEE Wireless Commun. Lett.*, to be published.
[8] M. Chen, M. Mozaffari, W. Saad, C. Yin, M. Debbah, and C. S. Hong, "Caching in the sky: Proactive deployment of cache-enabled unmanned aerial vehicles for optimized quality-of-experience," *IEEE J. Sel. Areas Commun.*, vol. 35, no. 5, pp. 1046–1061, May 2017.
[9] Z. M. Fadlullah, D. Takaishi, H. Nishiyama, N. Kato, and R. Miura, "A dynamic trajectory control algorithm for improving the communication throughput and delay in UAV-aided networks," *IEEE Netw.*, vol. 30, no. 1, pp. 100–105, Jan./Feb. 2016.
[10] A. Dhekne, M. Gowda, and R. R. Choudhury, "Cell tower extension through drones: Poster," in *Proc. ACM MobiCom*, 2016, pp. 456–457.
[11] C. Zhang and W. Zhang, "Spectrum sharing for drone networks," *IEEE J. Sel. Areas Commun.*, vol. 35, no. 1, pp. 136–144, Jan. 2017.
[12] A. Al-Hourani, S. Kandeepan, and S. Lardner, "Optimal LAP altitude for maximum coverage," *IEEE Wireless Commun. Lett.*, vol. 3, no. 6, pp. 569–572, Dec. 2014.
[13] M. Mozaffari, W. Saad, M. Bennis, and M. Debbah, "Mobile Internet of Things: Can UAVs provide an energy-efficient mobile architecture?" in *Proc. IEEE GLOBECOM*, Dec. 2016, pp. 1–6.
[14] P. Yang, X. Cao, C. Yin, Z. Xiao, X. Xi, and D. Wu, "Proactive drone-cell deployment: Overload relief for a cellular network under flash crowd traffic," *IEEE Trans. Intell. Transp. Syst.*, vol. 18, no. 10, pp. 2877–2892, Oct. 2017.
[15] R. I. Bor-Yaliniz, A. El-Keyi, and H. Yanikomeroglu, "Efficient 3-D placement of an aerial base station in next generation cellular networks," in *Proc. IEEE ICC*, May 2016, pp. 1–5.
[16] E. Kalantari, H. Yanikomeroglu, and A. Yongacoglu, "On the number and 3D placement of drone base stations in wireless cellular networks," in *Proc. IEEE VTC-Fall*, Sep. 2016, pp. 1–6.
[17] H. Zhou *et al.*, "TV white space enabled connected vehicle networks: Challenges and solutions," *IEEE Netw.*, vol. 31, no. 3, pp. 6–13, May/Jun. 2017.
[18] H. Zhou, B. Liu, L. Gui, X. Wang, and Y. Li, "Fast spectrum sharing for cognitive radio networks: A joint time-spectrum perspective," in *Proc. IEEE GLOBECOM*, Dec. 2011, pp. 1–5.
[19] Y. Zhou, N. Cheng, N. Lu, and X. S. Shen, "Multi-UAV-aided networks: Aerial-ground cooperative vehicular networking architecture," *IEEE Veh. Technol. Mag.*, vol. 10, no. 4, pp. 36–44, Dec. 2015.
[20] S. Zhang, G. Wang, and C.-L. I, "Is mmWave ready for cellular deployment?" *IEEE Access*, vol. 5, pp. 14369–14379, 2017.
[21] T. Nitsche, A. B. Flores, E. W. Knightly, and J. Widmer, "Steering with eyes closed: Mm-wave beam steering without in-band measurement," in *Proc. IEEE INFOCOM*, Apr./May 2015, pp. 2416–2424.
[22] D.-J. Deng, S.-Y. Lien, J. Lee, and K.-C. Chen, "On quality-of-service provisioning in IEEE 802.11ax WLANs," *IEEE Access*, vol. 4, pp. 6086–6104, 2016.
[23] Q. Ye and W. Zhuang, "Distributed and adaptive medium access control for Internet-of-Things-enabled mobile networks," *IEEE Internet Things J.*, vol. 4, no. 2, pp. 446–460, Apr. 2017.
[24] W. Xu, H. A. Omar, W. Zhuang, and X. S. Shen, "Delay analysis of in-vehicle Internet access via on-road WiFi access points," *IEEE Access*, vol. 5, pp. 2736–2746, 2017.
[25] H. Ghazzai, E. Yaacoub, M. S. Alouini, Z. Dawy, and A. Abu-Dayya, "Optimized LTE cell planning with varying spatial and temporal user densities," *IEEE Trans. Veh. Technol.*, vol. 65, no. 3, pp. 1575–1589, Mar. 2016.
[26] M. Clerc and J. Kennedy, "The particle swarm—Explosion, stability, and convergence in a multidimensional complex space," *IEEE Trans. Evol. Comput.*, vol. 6, no. 1, pp. 58–73, Feb. 2002.
[27] M. García-Fernández *et al.*, "Antenna diagnostics and characterization using unmanned aerial vehicles," *IEEE Access*, vol. 5, pp. 23563–23575, 2017.
[28] W. Shi, J. Li, W. Xu, H. Zhou, N. Zhang, and X. Shen, "3D drone-cell deployment optimization for drone assisted radio access networks," in *Proc. IEEE/CIC ICCC*, Oct. 2017, pp. 1–6.

WEISEN SHI received the B.S. degree from Tianjin University, Tianjin, China, in 2013, and the M.S. degree from the Beijing University of Posts and Telecommunications, Beijing, China, in 2016. He is currently pursuing the Ph.D. degree with the Department of Electrical and Computer Engineering, University of Waterloo, Waterloo, ON, Canada. His research interests include drone communication and networking, network function virtualization, and vehicular networks.

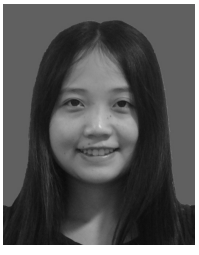

JUNLING LI received the B.S. degree from Tianjin University, Tianjin, China, in 2013, and the M.S. degree from the Beijing University of Posts and Telecommunications, Beijing, China, in 2016. She is currently pursuing the Ph.D. degree with the Department of Electrical and Computer Engineering, University of Waterloo, Waterloo, ON, Canada. Her research interests include software-defined networking, network function virtualization, and vehicular networks.

WENCHAO XU received the B.E. and M.E. degrees from Zhejiang University, Hangzhou, China, in 2008 and 2011, respectively. He is currently pursuing the Ph.D. degree with the Department of Electrical and Computer Engineering, University of Waterloo, Waterloo, ON, Canada. In 2011, he joined Alcatel Lucent Shanghai Bell Co., Ltd., where he was a Software Engineer of telecom virtualization. His research interests include wireless communications with emphasis on resource allocation, network modeling, and mobile data offloading.

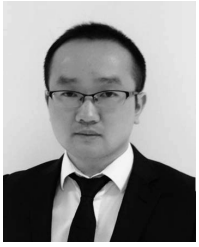

HAIBO ZHOU received the Ph.D. degree in information and communication engineering from Shanghai Jiao Tong University, Shanghai, China, in 2014. From 2014 to 2017, he was a Post-Doctoral Fellow with the Broadband Communications Research Group, ECE Department, University of Waterloo, Waterloo, ON, Canada. He is currently an Associate Professor with the School of Electronic Science and Engineering, Nanjing University. His research interests include resource management and protocol design in cognitive radio networks and vehicular networks.

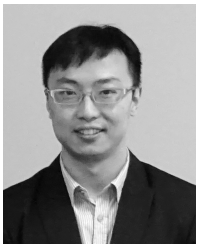

NING ZHANG received the Ph.D. degree from the University of Waterloo, Waterloo, ON, Canada, in 2015. He is currently an Assistant Professor with the Department of Computing Science, Texas A&M University-Corpus Christi. He was a Post-Doctoral Research Fellow with the University of Waterloo and then with the University of Toronto. His current research interests include next generation wireless networks, software-defined networking, vehicular networks, and physical layer security. He was a co-recipient of the best paper awards at the IEEE GLOBECOM 2014 and the IEEE WCSP 2015.

SHAN ZHANG (S'13–M'16) received the B.S. degree from the Department of Information, Beijing Institute Technology, Beijing, China, in 2011, and the Ph.D. degree from the Department of Electronic Engineering, Tsinghua University, Beijing, in 2016. She is currently with the School of Computer Science and Engineering, Beihang University, Beijing. From 2016 to 2017, she was a Post-Doctoral Fellow with the Department of Electrical and Computer Engineering, University of Waterloo, Waterloo, ON, Canada. Her research interests include network resource and traffic management, network virtualization and integration. She received the Best Paper Award at the Asia–Pacific Conference on Communication in 2013.

XUEMIN (SHERMAN) SHEN (M'97–SM'02–F'09) received the B.Sc. degree from Dalian Maritime University, China, in 1982, and the M.Sc. and Ph.D. degrees from Rutgers University, New Brunswick, NJ, USA, in 1987 and 1990, respectively, all in electrical engineering. He is currently a Professor and the University Research Chair with the Department of Electrical and Computer Engineering, University of Waterloo, Canada. He is also the Associate Chair for Graduate Studies. His research interests include resource management in interconnected wireless/wired networks, wireless network security, social networks, smart grid, and vehicular ad hoc and sensor networks. He is an elected member of the IEEE ComSoc Board of Governor and the Chair of the Distinguished Lecturers Selection Committee. He served as the Technical Program Committee Chair/Co-Chair for the IEEE Globecom '16, Infocom '14, IEEE VTC '10 Fall, and Globecom '07, the Symposia Chair for the IEEE ICC '10, the Tutorial Chair for the IEEE VTC '11 Spring and the IEEE ICC '08, the General Co-Chair for the ACM Mobihoc '15, Chinacom '07, and QShine '06, and the Chair for the IEEE Communications Society Technical Committee on Wireless Communications and P2P Communications and Networking. He received the Excellent Graduate Supervision Award in 2006, and the Outstanding Performance Award in 2004, 2007, 2010, and 2014 from the University of Waterloo, the Premier's Research Excellence Award in 2003 from the Province of Ontario, Canada, and the Distinguished Performance Award in 2002 and 2007 from the Faculty of Engineering, University of Waterloo. He is a registered Professional Engineer in Ontario, Canada, an Engineering Institute of Canada Fellow, a Canadian Academy of Engineering Fellow, a Royal Society of Canada Fellow, and a Distinguished Lecturer of the IEEE Vehicular Technology Society and Communications Society. He also serves/served as the Editor-in-Chief for the IEEE Network, *Peer-to-Peer Networking and Application*, *IET Communications*, and the IEEE Internet of Things Journal, a Founding Area Editor for the IEEE Transactions on Wireless Communications, an Associate Editor for the IEEE Transactions on Vehicular Technology, *Computer Networks*, and *ACM/Wireless Networks*, and a Guest Editor for the IEEE Journal on Selected Areas in Communications, the IEEE Wireless Communications, the *IEEE Communications Magazine*, and *ACM Mobile Networks and Applications*.